

Nonlinear cavity optomechanics with nanomechanical thermal fluctuations

Rick Leijssen¹, Giada La Gala¹, Lars Freisem¹, Juha T. Muhonen¹,
and Ewold Verhagen^{1,*}

¹Center for Nanophotonics, AMOLF, Science Park 104, 1098 XG,
Amsterdam, The Netherlands

*corresponding author: verhagen@amolf.nl

April 13, 2018

Abstract

The inherently nonlinear interaction between light and motion in cavity optomechanical systems has experimentally been studied in a linearized description in all except highly driven cases. Here we demonstrate a nanoscale optomechanical system, in which the interaction between light and motion is so large (single-photon cooperativity $C_0 \approx 10^3$) that thermal motion induces optical frequency fluctuations larger than the intrinsic optical linewidth. The system thereby operates in a fully nonlinear regime, which pronouncedly impacts the optical response, displacement measurement, and radiation pressure backaction. Experiments show that the apparent optical linewidth is dominated by thermomechanically-induced frequency fluctuations over a wide temperature range. The nonlinearity induces breakdown of the traditional cavity optomechanical descriptions of thermal displacement measurements. Moreover, we explore how radiation pressure backaction in this regime affects the mechanical fluctuation spectra. The strong nonlinearity could serve as a resource to control the motional state of the resonator. We demonstrate the use of highly nonlinear transduction to perform a quadratic measurement of position while suppressing linear transduction.

1 Introduction

In cavity optomechanics, the interaction between light in an optical cavity and the motion of a mechanical resonator enables sensitive optical readout of displacement, as well as manipulation of the resonator's motion through optical forces¹. This has allowed demonstrations of sideband and feedback cooling of the mechanical resonator near its quantum ground state^{2–5}, squeezing of light^{6–8} and of the mechanical zero-point fluctuations^{9–11}, entanglement¹² and state transfer¹³ between the optical and mechanical degrees of freedom, as well as detection of radiation pressure shot noise^{14,15} and non-classical correlations^{16–19}. In all of these examples, the coupling between fluctuations of the optical field and the mechanical displacement can be regarded as linear for all intents and purposes.

However, the optomechanical interaction is inherently nonlinear. Indeed, the cavity optomechanical interaction Hamiltonian reads $\hat{H}_{\text{int}} = -\hbar g_0 \hat{a}^\dagger \hat{a} \hat{x} / x_{\text{zpf}}$, where \hat{a} is the annihilation operator for the optical cavity field, and \hat{x} is the displacement operator for the mechanical resonator. The photon-phonon coupling rate $g_0 = (\partial\omega_c/\partial x)_{x_{\text{zpf}}}$ quantifies the change of the cavity frequency ω_c due to a displacement the size of the resonator's zero-point fluctuations x_{zpf} . This interaction Hamiltonian leads to nonlinear behavior, as the equations of motion it generates contain products of two operators. The linearized form of the interaction $\hat{H}_{\text{int}} = -\hbar g_0 \bar{\alpha} (\delta\hat{a}^\dagger + \delta\hat{a}) \hat{x} / x_{\text{zpf}}$ does not contain the nonlinear terms, but usually suffices to describe the dynamics of fluctuations¹. This form emerges when the cavity field is written as the sum $\hat{a} = \bar{\alpha} + \delta\hat{a}$ of an average coherent field $\bar{\alpha}$ and fluctuations $\delta\hat{a}$, and the term containing $\delta\hat{a}^\dagger \delta\hat{a} \hat{x}$ is neglected by assuming $\delta\hat{a} \ll \bar{\alpha}$. The linearization is generally valid in the presence of a strong optical drive. However, the assumption that $\delta\hat{a} \ll \bar{\alpha}$ is not valid if mechanical fluctuations shift the cavity completely in and out of resonance with the optical drive, i.e. when they produce a cavity frequency shift comparable to the optical linewidth κ . Then, nonlinear processes become crucially important, and qualitatively different effects can occur.

In the quantum domain, intriguing implications of this nonlinearity are expected in the single-photon strong-coupling regime, when the coupling rate g_0 exceeds the optical and mechanical loss rates κ and Γ , respectively. There, quantum-level mechanical fluctuations induce a nonlinear response, creating nonclassical states of both light and motion when the mechanical frequency Ω_m approaches the optical linewidth as well^{20–22}. In the so-called bad-cavity limit ($\kappa > \Omega_m$), the nonlinearity of the interaction provides a useful path towards creating motional quantum states, e.g. through performing quadratic measurements of displacement (proportional to \hat{x}^2)^{23–27}.

In macroscopic or chip-based optomechanical implementations, the breakdown of linearity when $\delta\hat{a} \gtrsim \bar{\alpha}$ has so far only been experimentally relevant for mechanical resonators driven to large amplitude, e.g. through optomechanical parametric amplification. In that case, nonlinear effects determine the maximum amplitude of optomechanical self-oscillation^{1,28–32}, and can lead to complex nonlinear dynamical phenomena such as chaos^{33–35}.

Here, we establish and explore the regime where even intrinsic Brownian motion induces cavity frequency fluctuations larger than the optical linewidth. In this regime, the nonlinear nature of the cavity optomechanical interaction becomes important in all essential phenomena, including optomechanical displacement measurement and radiation pressure backaction. The regime is de-

fined by $g_0\sqrt{2\bar{n}_{\text{th}}} \gtrsim \kappa$, where $\bar{n}_{\text{th}} = k_B T / \hbar \Omega_m$ is the average phonon occupancy of the mechanical mode with frequency Ω_m , in thermal equilibrium at a temperature T . It is clear from this condition that any optomechanical system in which the ratio g_0/κ is increased will enter this regime before reaching the single-photon strong-coupling regime, unless the mechanical resonator is pre-cooled to its ground state. The condition can equivalently be expressed as $C_0 \gtrsim \kappa/\gamma$, i.e. the single-photon cooperativity $C_0 \equiv 4g_0^2/\kappa\Gamma$ being larger than the ratio of optical decay rate and mechanical thermal decoherence rate $\gamma \equiv \Gamma\bar{n}_{\text{th}}$. In our experiments, we follow a strategy of exploiting subwavelength optical confinement³⁶ to reach unprecedented single-photon cooperativity around 10^3 ; two to three orders of magnitude larger than typical values in nanoscale optomechanical systems to date^{1,37,38}, and only comparable with cold-atom implementations^{15,39}. In the systems demonstrated here, the apparent optical linewidth is dominated by the transduced thermal motion over a wide range of temperatures, and the transduction becomes extremely nonlinear. We numerically implement a model that describes transduction in this regime, in contrast to the conventional analytical description, which fails for fluctuations that approach the linewidth. Moreover, we analyze how the nonlinear response of the radiation pressure force to stochastic fluctuations alters the shape of mechanical fluctuation spectra. Finally, we provide a proof-of-concept demonstration of exploiting the nonlinearity to conduct sensitive quadratic readout of nanomechanical displacement.

2 Results

2.1 Sliced photonic crystal nanobeam

Figure 1a shows the optomechanical system we employ. It combines low-mass, MHz-frequency, nanomechanical modes with subwavelength optical field confinement in a sliced photonic crystal nanobeam³⁶, to establish strong optomechanical interactions with photon-phonon coupling rates g_0 in the range of tens of MHz. The fundamental mechanical resonance of the sliced nanobeam, shown in Fig. 1b, strongly influences the gap distance d in the middle of the beam. The motion of the resonator in this mechanical mode is associated with a simulated effective mass of 1.5 pg, leading to relatively large zero-point fluctuations $x_{\text{zpf}} = \sqrt{\hbar/2m\Omega_m} = 43$ fm. As shown in the optical field profile of the fundamental cavity resonance of the structure in Fig. 1c, the nanoscale gap in the middle of the beam confines the light to a small area, which makes the optical cavity resonance frequency ω_c strongly dependent on the gap size d between the two halves of the nanobeam. With the fabricated gap size of 45–50 nm, we simulated the optical frequency change due to a displacement of the beams to be $\partial\omega/\partial x = 0.8$ THz/nm, where $x \equiv d/2$. This leads to an expected optomechanical coupling rate of $g_0/2\pi = 35$ MHz. We decrease the optical cavity decay rate and increase the outcoupling at normal incidence by engineering the angular radiation spectrum of the sliced nanobeam structure^{40,41} (see Methods). The resultant simulated optical decay rate is 8.8 GHz, showing that the sliced nanobeam design is capable of combining large optomechanical interactions with low optical losses.

We employ a balanced homodyne detection scheme, schematically shown in Fig. 1d, to study the fluctuations imparted on the light in the nanobeam cav-

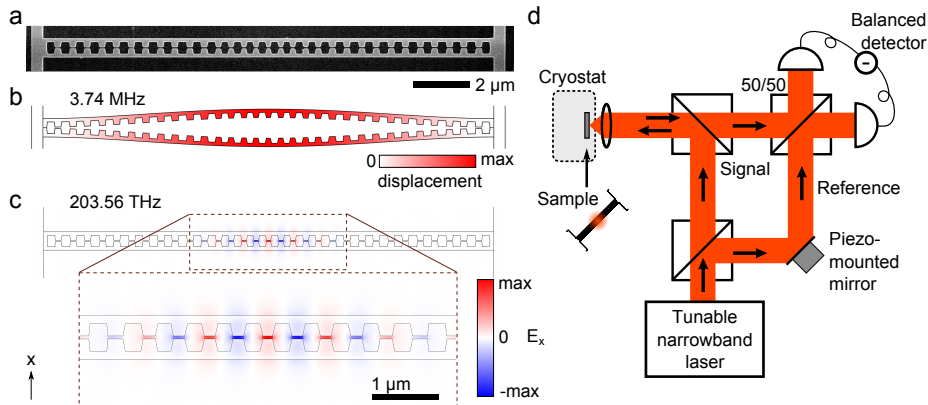


Figure 1 | Structure and setup. (a) Electron microscope image of a silicon sliced nanobeam. The shown part is free-standing and has a thickness of 250 nm. The scale bar is valid for panels (a–c). (b) Simulated displacement profile of the fundamental mechanical resonance, which strongly modifies the gap size. (c) Simulated transverse electric field of the fundamental optical cavity resonance. The inset shows an enlarged view of the cavity region, formed by a tapered variation of the distances between, and sizes of, the holes. (d) Schematic diagram of the employed balanced homodyne interferometer measurement setup. The reflection from the sliced nanobeam is interfered with the light from the reference arm, enabling near-quantum-limited measurement of fluctuation spectra even with low power incident on the sample (see Methods for details).

ity through the optomechanical interaction (see Methods). Figure 2a depicts fluctuation spectra recorded with an electronic spectrum analyser, showing the two fundamental mechanical resonances of one device, measured at 3 K with the laser on-resonance with the cavity. We ascribe the two resonances to the two half-beams moving at slightly different natural frequencies. The fact that in this device the two resonances are nearly of equal strength indicates that the two half-beams are mechanically coupled at a rate smaller than their intrinsic frequency difference³⁶, and thus moving approximately independent of each other: stronger mechanical coupling would result in hybridization of the resonances into symmetric and antisymmetric eigenmodes with different optical transduction strengths.

2.2 Modification of optical response

The signal strength of the transduced motion around the cavity resonance wavelength of 1457.5 nm, measured at 3 K and at room temperature, is shown in Fig. 2b as a function of laser detuning. The fluctuations are recorded while continuously sweeping the piezo-mounted mirror over multiple interferometer fringes, thus averaging the measured signal quadratures. As we analyze in detail elsewhere⁴², the resulting signal strength acquires a simple single-peaked detuning dependence with a maximum for the laser tuned to the cavity resonance (see also Appendix). As Fig. 2b shows, the apparent linewidth of the optical resonance is strongly influenced by temperature. We infer from this that the frequency fluctuations of the cavity due to the thermal motion of the mechan-

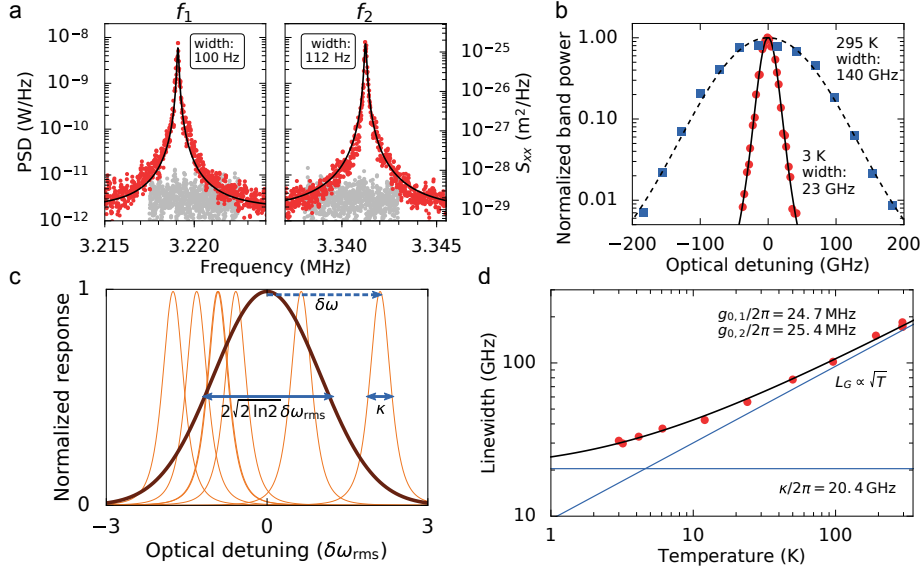


Figure 2 | Optical linewidth broadening. (a) Recorded optically measured spectra of the two fundamental mechanical resonances (PSD: power spectral density, optical power incident on sample: 11.3 nW). Grey noise spectra were recorded with the signal arm of the interferometer blocked. Black lines show the lorentzian fit, used to determine the linewidths (full width at half maximum) shown in the figure. The displacement spectral density scale on the right-hand side assumes linear transduction of the known thermal motion of the structure at the cryostat temperature. (b) Detuning dependence of the measured transduced thermal motion, measured as the band power at the fundamental mechanical frequency, at room temperature and at 3 K. The black solid and dashed lines show fits with a Voigt lineshape squared (see Methods), with the widths (full width at half maximum) shown. (c) Schematic representation of thermal motion-induced linewidth broadening: the thin orange lines represent the intrinsic cavity response at a few example detunings, while the thick brown line shows the overall response resulting from averaging over the fluctuating detuning. (d) Optical linewidth versus temperature. The solid line is a fit with a model that assumes a constant lorentzian intrinsic linewidth κ convolved with a gaussian with a width L_G that depends on \sqrt{T} (details in text). The asymptotes of the fit function allow us to extract κ and the optomechanical coupling rate g_0 , shown in the graph.

ical resonator dominate the response, which occurs when they are larger than the intrinsic optical linewidth. This is illustrated in Fig. 2c: While the intrinsic optical response of the cavity is Lorentzian with linewidth κ (orange thin lines), the distribution of cavity frequency fluctuations due to thermal motion has a Gaussian spectrum (brown thick line), whose linewidth L_G is related to the root-mean-square value of the frequency fluctuations $\delta\omega_{\text{rms}}$, as $L_G = 2\sqrt{2\ln 2}\delta\omega_{\text{rms}}$. In the bad-cavity limit we consider here, we model the observed cavity response as a Voigt lineshape, which is a convolution between the Lorentzian cavity response and the Gaussian distribution of cavity resonance frequencies due to the Brownian motion. We note that the measured electronic power spectral density is proportional to the square of the optical response, which leads to a smaller apparent linewidth in the detuning dependence shown in Fig. 2b. In the following, we only report the extracted linewidth (see Methods), which directly corresponds to the optical loss rate κ in the low-temperature limit, and the full width at half maximum of the frequency fluctuation distribution in the high-temperature limit.

As the thermomechanical displacement variance is given by $\langle x_{\text{th}}^2 \rangle = 2\bar{n}_{\text{th}}x_{\text{zpf}}^2$, the induced frequency fluctuations due to a single mechanical mode at frequency Ω_{m} are characterized by a root-mean-square amplitude

$$\delta\omega_{\text{rms}} \equiv \sqrt{\langle \delta\omega^2 \rangle} = g_0\sqrt{2\bar{n}_{\text{th}}} = g_0\sqrt{2k_B T/\hbar\Omega_{\text{m}}}, \quad (1)$$

which reveals a square-root dependence on temperature. In case multiple independent mechanical modes are coupled to the optical cavity, the variances of the cavity frequency fluctuations are added, i.e. $\delta\omega_{\text{rms}}^2 = \sum_j \langle \delta\omega_j^2 \rangle$, which preserves the overall temperature dependence. Fig. 2d shows the full measured temperature dependence of the apparent linewidth, which exhibits the expected square-root dependence on temperature at the higher temperatures. We fit the datapoints using an equation that approximates the linewidth of the Voigt lineshape (see Methods), with a fixed Lorentzian contribution due to the intrinsic optical loss and a Gaussian contribution that follows Eq. 1. The resulting fit curve is shown in Fig. 2d, together with its asymptotes (thin blue lines). These asymptotes allow us to directly extract the intrinsic optical linewidth κ and the variance of thermal motion-induced frequency fluctuations of the cavity, without further calibration. There are two mechanical resonances that show significant coupling to the optical cavity resonance as shown in Fig. 2a, and we derive the ratio between their coupling strengths from the ratio between the signal strengths at the two mechanical resonance frequencies³⁶. Using this ratio and the measured resonance frequencies, we obtain $g_0/2\pi = 24.7$ MHz and 25.4 MHz for the two mechanical modes.

This unprecedented optomechanical coupling rate, combined with the extracted optical decay rate of $\kappa/2\pi = 20.4$ GHz and the mechanical decay rate of $\Gamma/2\pi = 100$ Hz, means that this device has a single-photon cooperativity $C_0 = 4g_0^2/\kappa\Gamma = 1.1 \times 10^3$. The single-photon cooperativity is a regularly used metric that combines optomechanical coupling and losses^{1,38}. It signals the inverse of the average number of intracavity photons that would be needed to perform a measurement at the standard quantum limit, if all photons escaping the cavity could be employed towards such a measurement. Interestingly, the combination of quadrature-averaged detection with temperature-dependent linewidth measurement allows direct extraction of C_0 , with no other calibration

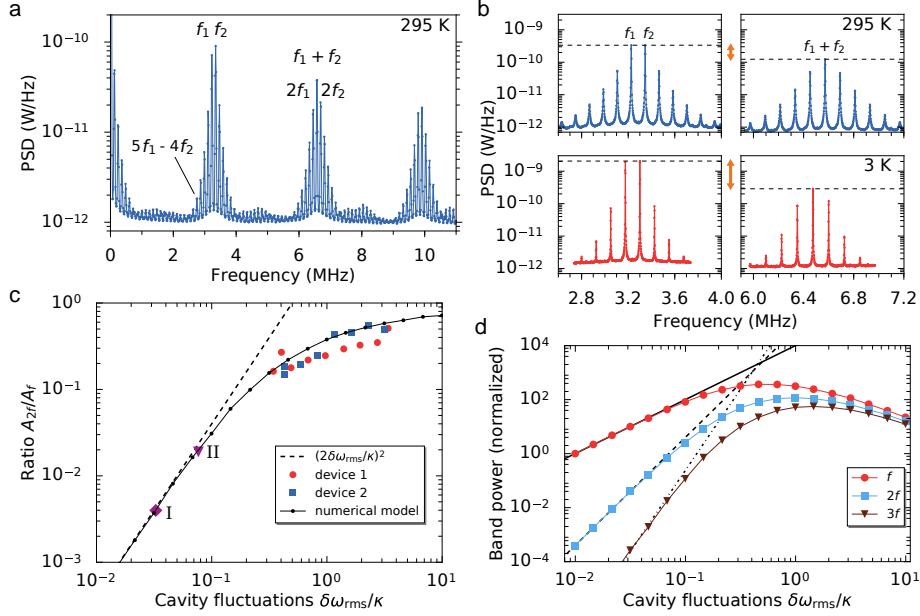


Figure 3 | Nonlinear transduction. (a) Power spectral density of transduced thermal motion, measured at room temperature (295 K). (b) Power spectral density of the group of peaks around f_1, f_2 and around $f_1 + f_2$, at room temperature (top) and at 3 K (bottom). (c) Ratio between the 3 second-order peaks around $f_1 + f_2$ and the peaks at the fundamental frequencies f_1, f_2 as a function of the relative cavity fluctuations $\delta\omega_{\text{rms}}/\kappa$. Device 1 is the same device presented in the other figures; device 2 is a similar device with different parameters (see text); room-temperature measurements from two recent publications are indicated with datapoints I (ref. [24]) and II (ref. [36]). The dashed line indicates the prediction from an analytical model with an order-by-order approximation, while the black datapoints connected with solid lines represent a calculation based on a numerically generated timetrace to simulate thermal motion. (d) Expected band power at the fundamental frequency f as well as at $2f$ and $3f$, as a function of the relative cavity fluctuations. Solid, dashed, and dash-dotted lines follow the order-by-order approximation, while the colored points are the outcome of our numerical model.

than that of the temperature of the mechanical bath. The extremely high value we report here, which exceeds previously reported nano-optomechanical architectures by 2 to 3 orders of magnitude^{1,37,38}, highlights the prospects of such systems for measurement-based quantum control of motion.

2.3 Nonlinear transduction

When the relative cavity fluctuations $\delta\omega_{\text{rms}}/\kappa$ are large, a typical mechanical oscillation samples the full width of its Lorentzian lineshape. Since this lineshape is nonlinear, higher-order harmonics are expected to appear in the transduced optical fluctuation spectrum. At room temperature, the cavity frequency fluctuations due to both mechanical modes have an amplitude $\delta\omega_{\text{rms}} = \left(2\sum_j \bar{n}_{\text{th},j} g_{0,j}^2\right)^{1/2} = 2\pi \times 69 \text{ GHz} \approx 3.4\kappa$. As shown in Fig. 3a, at room tem-

perature the measurement signal indeed contains fluctuations at (mixed) integer multiples of the two fundamental mechanical resonances, i.e. $f_{j,k} = |jf_1 \pm kf_2|$, where $j, k \in \{0, 1, 2, \dots\}$. Around the fundamental frequencies near 3.3 MHz, we observe odd mixing terms up to 9th order (e.g. a peak is visible at $f_{5,-4} = 5f_1 - 4f_2$), and around the sum frequency at 6.6 MHz, even mixing terms up to 10th order can be identified.

At a temperature of 3 K, the ratio between the cavity frequency fluctuations, caused by both mechanical modes, and the intrinsic optical linewidth is $\delta\omega_{\text{rms}}/\kappa = 0.34$, which still leads to significant higher-order transduction. Fig. 3b shows a direct comparison of the spectra obtained at room temperature and at 3 K. As a measure for the higher-order transduction, we take the ratio between the second- and first-order transduction. We expect the ratio between the orders to be independent of other parameters, such that it gives direct insight in the strength of the nonlinearity. This ratio is clearly larger at higher temperature (the inverse of the ratio is indicated with arrows in Fig. 3b).

Higher-order transduction has previously been described with an analytical model that is based on a Taylor expansion of the measurement output around the average detuning^{23,24,36}. For small frequency modulation, the higher-order terms in this expansion can be approximated as independent. Mathematically, this is based on an order-by-order approximation $(\cos \Omega_m t)^n \approx 2^{-(n+1)} \cos n\Omega_m t$. The resulting expression for the maximum signal power measured at the (multiple of the) resonance frequency $k\Omega$ is

$$\langle P^2 \rangle_{k\Omega} = 2A^2 k! \left(\frac{2\langle \delta\omega^2 \rangle}{\kappa^2} \right)^k, \quad (2)$$

where A is a constant factor that depends on the optical power used as well as the coupling efficiency to the cavity (for details, see Appendix and ref. [42]).

In Fig. 3c, the dashed line shows the ratio between the second- and first-order transduction that follows from this order-by-order approximation, $(2\delta\omega_{\text{rms}}/\kappa)^2$. The datapoints labeled I and II, which represent room-temperature measurements reported in refs. [24] and [36], respectively, are still well-explained by the order-by-order approximation. For the devices under study, $\delta\omega_{\text{rms}}/\kappa$ is so large that this approach breaks down. This is shown by our temperature sweep data, where we take the fitted area A_{f_j} under the peaks at the fundamental frequency and at twice the fundamental frequency (labeled in Fig. 3a), and plot their ratio: $(A_{2f_1} + A_{f_1+f_2} + A_{2f_2})/(A_{f_1} + A_{f_2})$. The red circles indicate the results for the same device presented in the other figures, while the blue squares represent a different device with $g_0/2\pi = 10.8$ MHz and $\kappa/2\pi = 9.0$ GHz.

Where the order-by-order approximation breaks down, the nonlinear transduction still follows the prediction of our full model, in which we calculate the expected homodyne output from a numerical time-domain simulation of the thermal motion (see Methods). We then Fourier transform the simulated signal and plot the ratio of the band powers, noting that the numerical result does not depend on whether we include one or two mechanical resonances when plotted against total relative cavity fluctuations $\delta\omega_{\text{rms}}/\kappa$. This full model prediction is shown with the black dots connected by solid lines in Fig. 3c. The numerical simulation follows the experimentally observed trend, and shows that the ratio between second- and first-order transduction saturates close to unity at higher fluctuation amplitudes. It is important to note that only such a numerical ap-

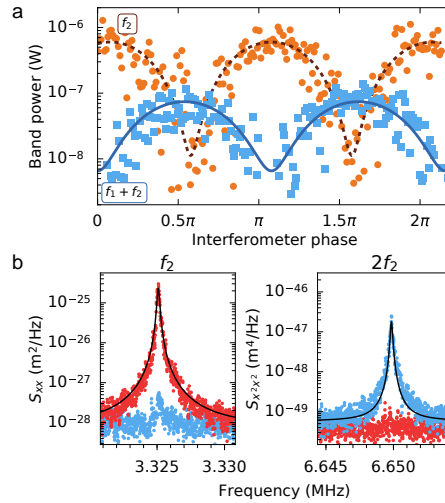


Figure 4 | Quadratic measurement. (a) Transduction of first and second order peaks (orange and lightblue datapoints, respectively) while sweeping the piezo mirror position, with 10.5 nW optical power incident on the sample. The horizontal scale was derived from the sinusoidal fit to the band power of f_2 shown in the figure, and the data at $f_1 + f_2$ was shifted horizontally by about 3% to compensate for measurement drift. (b) Spectra at f_2 and $2f_2$ at optimal mirror positions for linear and quadratic transduction (red and lightblue datapoints, respectively), taken with 12.8 nW of incident optical power. The black solid lines are Lorentzian fits, whose area was used to calibrate the vertical scale.

proach correctly takes into account the statistics of the transduced motion: the strongly nonlinear conversion of displacement to optical field precludes an analysis based solely on one or several moments of the displacement distribution. In other words, a single peak in the fluctuation spectrum at $k\Omega_m$ can no longer be dominantly associated with a specific scattering process involving k phonons, but also contains contributions due to $k + 2, k + 4, \dots$ phonons.

Using the numerical model, we calculate the absolute signal power due to thermal motion at the fundamental frequency f and its multiples $2f$ and $3f$ (points in Fig. 3d).

For cavity frequency fluctuations $\delta\omega_{\text{rms}}/\kappa$ larger than about 10%, both linear and higher-order transduction no longer follow the order-by-order approximation given in equation 2 (black lines), which predicts monotonic increases in signal strength. Instead, we recognize an optimum single-harmonic signal strength due to cavity frequency fluctuations, beyond which larger fluctuations cause the cavity to be off-resonance most of the time. This reduces the transduction at a single harmonic in the optical signal, instead distributing energy equally among an increasing number of harmonics as the system operates deeper in the nonlinear regime.

2.4 Quadratic measurement of motion

A measurement that is directly sensitive to the square of displacement, x^2 , is proportional to the energy of the mechanical resonator. Displacement-squared

optomechanical coupling hence provides a means to perform quantum non-demolition measurements of phonon number^{43–47}. With sufficiently suppressed linear backaction, measurements of x^2 have been proposed as a possible route to preparing non-classical states of motion of the mechanical resonator, conditional on the outcome of such a nonlinear measurement^{23,24,48}. Nonlinear transduction allows measurements of x^2 by detecting the transduced motion at twice the fundamental frequency, $2f$. This gives rise to an effective quadratic coupling rate given by g_0^2/κ (ref. [48]), which amounts to $2\pi \times 32$ kHz in the device presented here. To put that number in perspective, one can compare it to the quadratic coupling rate $\mu_0 = (\partial^2\omega_c/\partial x^2)x_{\text{zpf}}^2$ in devices in which the frequency is not linearly dependent on the displacement. A state-of-the-art double-slotted photonic crystal system recently demonstrated⁴⁶ a quadratic coupling rate of $\mu_0/2\pi = 245$ Hz.

In Fig. 4 we exploit the large nonlinear transduction in our device to show selective linear and quadratic measurements of mechanical displacement at 3 K. Figure 4a shows the strength of the first- and second-order transduction (proportional to x and x^2 , respectively) as a function of the piezo mirror position that controls the homodyne phase, which is now no longer continuously swept. The data follows the expected sinusoidal dependence, as evidenced by the fits shown with solid lines.

We obtained the spectra in Fig. 4b by positioning the piezo mirror at the optimum points for first- and second-order transduction, depicted by the red and blue datapoints respectively. The vertical scale was calibrated by using the order-by-order approximation, where the area under the peaks in the spectrum is proportional to the variance of the thermal motion of the structure, which here provides a lower limit for the sensitivity. This analysis yields an imprecision for the displacement-squared measurement of 2.0×10^{-25} m²/Hz^{1/2}. With the current mechanical linewidth and this level of imprecision we would be able to measure a phonon occupation of 752 with a signal-to-noise ratio of 1, which is an improvement over the measurement sensitivity in the proof-of-concept experiment reported in ref. [24] by approximately a factor 50. In the data shown here, the suppression of linear transduction is 28 dB, which could be further improved by implementing a feedback loop to lock the homodyne interferometer phase to a desired value.

It is important to note that our numerical model, as shown in Fig. 3d, predicts second-order transduction at only 10% of the strength of the order-by-order approximation for $\delta\omega_{\text{rms}}/\kappa \approx 0.34$, which is the size of the relative cavity fluctuations in our device at 3 K. Therefore, we expect that if this device is cooled further, to the point where the order-by-order approximation accurately predicts the transduction, an even lower imprecision noise of 6.3×10^{-26} m²/Hz^{1/2} would be recovered without any further optimization. This would correspond to measuring a phonon occupation of 238 with unity signal-to-noise. In the regime where the order-by-order approximation holds, this phonon occupation detection limit for quadratic measurement scales as

$$\frac{1}{\bar{n}_{\text{min}}} = 16 \left(\frac{g_0}{\kappa}\right)^2 \eta \sqrt{\frac{P_{\text{in}}/\hbar\omega_c}{\Gamma}}, \quad (3)$$

with η the coupling efficiency to our cavity, and P_{in} the incident optical power (see Appendix). This allows estimating what improvements we need to reach

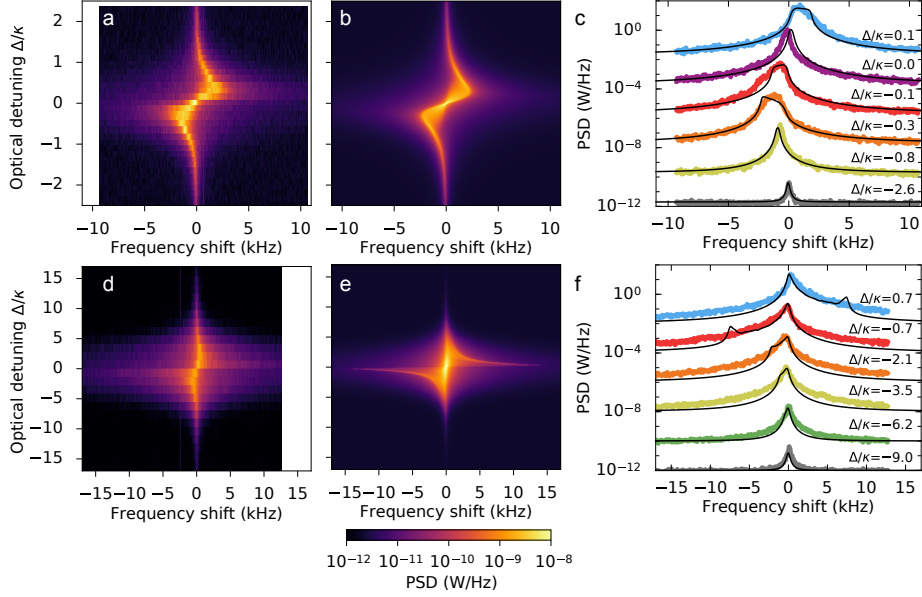


Figure 5 | Optical spring effect modified by large cavity frequency fluctuations. (a,d) Experimental spectrograms, showing transduced mechanical spectra (horizontal axis) versus the optical laser frequency (vertical axis), at two different experimental conditions: (a) cooled at 3 K, incident laser power 20.6 nW; (d) room temperature, 295 K, with incident laser power 124 nW. (b,e) Simulated spectrograms corresponding to those shown in (a,d), obtained by calculating frequency shifts for a large number of motional amplitudes sampled from a thermal distribution, and averaging Lorentzian lineshapes with center frequencies given by the calculated shifts (see text for details). The colorbar below panel (e) is shared for all the spectrograms (PSD: power spectral density). (c,f) Individual spectra at various detunings, overlaid with the corresponding simulated spectrum. Spectra were offset by a factor of 10^2 between them to avoid overlap.

$\bar{n}_{\min} \approx 1$, or a sensitivity that enables performing a measurement of phonon number near the quantum limit. This would for example be reached by improvements in g_0 and κ by factors of $\sqrt{2}$ and 2, respectively, as well as increasing the light collection efficiency η to 40% from the 1.3% estimated in the current device (see Appendix), by employing waveguide-based coupling strategies⁴⁹. This shows that with modest improvements of the device design and changes in the detection method, achieving quadratic measurement with an imprecision near the quadratic zero-point fluctuations is within reach.

2.5 Radiation pressure force with large cavity frequency fluctuations

The nonlinear regime not only impacts optical transduction of motion, but also pronouncedly affects the mechanical fluctuations themselves through its influence on radiation pressure backaction. The strongest manifestation of backaction in the regime where the cavity reacts nearly instantaneously to the mechanical motion ($\kappa \gg \Omega_m$) is the *optical spring effect*, which alters the mechanical reso-

nance frequency depending on the detuning between a drive laser frequency and the cavity resonance¹. Figure 5a and d show experimentally obtained spectrograms at low temperature (3 K, incident optical power 20.6 nW) and at room temperature (295 K, incident optical power 124 nW) around the fundamental harmonic of one of the mechanical modes, while Fig. 5c and f show several crosscuts at selected detunings. At low temperature, the observed effect is very similar to the normal (linearized) optical spring effect, where a blue detuned laser shifts the mechanical frequency upwards and vice versa for red detuning. However, we additionally observe a broadening of the obtained spectra both when the laser is red- and blue-detuned by ~ 10 GHz ($\kappa/2$). At room temperature, the spectra also become asymmetric: instead of a symmetric Lorentzian lineshape, the peak in spectra close to the optical resonance has a much steeper edge on one side than on the other side. In addition, the shift of the peak due to the optical spring effect scales linearly with the incident optical power, but the dataset at room temperature shows a smaller, rather than a larger shift than the dataset at 3 K, even though the used optical power is 5 times higher.

To account for these observations, we again need to take the large fluctuations of the cavity frequency due to thermal motion into consideration. The typical optomechanical model for the optical spring effect is based on the linearized equations of motion¹, which don't apply in the nonlinear regime we reach here. Instead, we calculate an effective spring constant from the first Fourier coefficient of the radiation pressure force, while the resonator oscillates harmonically, $x(t) = x_0 \cos \Omega t$. For this, we express the radiation pressure force in the cavity as

$$F_{\text{rad}} = \frac{\hbar(\partial\omega_c/\partial x)n_c^{\text{max}}}{1 + u^2}, \quad (4)$$

where $u \equiv \frac{2}{\kappa}(\bar{\Delta} + (\partial\omega_c/\partial x)x)$ with $\bar{\Delta}$ the average detuning between the laser and cavity frequency, and n_c^{max} is the maximum number of photons in the cavity when it is driven at resonance. The effective spring constant can be directly rescaled to obtain the frequency shift (see Appendix). As before, we numerically sample a thermal distribution to model the behaviour of the system, in this case by averaging over a large number of different amplitudes x_0 . Finally, we average a large number of Lorentzian lineshapes with the center frequencies given by the simulated frequency shifts and their widths set by the median linewidth measured in the experiment. The resulting simulated spectra are shown in Fig. 5b,e and plotted as black solid lines in Fig. 5c,f. To allow overplotting the simulated spectra with the experimental crosscuts, we rescaled all the simulated spectra such that the maximum value of the spectrum closest to resonance matched the experimental value. The model reproduces the broadening of the peaks as well as the asymmetry for the high-temperature data. At room temperature, a strong edge at larger frequency shifts is observed in the model, which is absent in the measurements. We attribute this to the presence of the other mechanical mode, which will tend to soften this effect. An interesting feature in this model is that the spectra obtained with the laser on-resonance are not affected at all, and we indeed observed experimentally that at $\bar{\Delta}/\kappa = 0$ the effect is much smaller if not entirely absent.

3 Discussion

Our analysis of both nonlinear transduction and backaction relies on a numerical model instead of an analytical description, as the typical order-by-order approximation to describe transduction breaks down at large relative cavity fluctuation strengths. This breakdown is related to the fact that the Taylor expansion used to describe the intracavity field²⁴ as a function of the relative detuning $u \equiv \frac{2}{\kappa}(\bar{\Delta} + \delta\omega)$,

$$a = \frac{\sqrt{n_c^{\max}}}{1 + iu} \approx \sqrt{n_c^{\max}}(1 - iu - u^2 + iu^3 + u^4 \dots), \quad (5)$$

does not converge for $|u| > 1$. For example, at average detuning $\bar{\Delta} = 0$, $u = 2\delta\omega/\kappa$ represents the cavity frequency fluctuations due to the thermal motion, meaning the power series does not converge when the mechanical motion changes the cavity frequency by more than a linewidth. Therefore, this model cannot be used to extrapolate the expected sensitivity of optomechanical measurements in the nonlinear regime we describe here. Our numerical model relies on a direct calculation of the optical response to mechanical motion, which can be performed for any cavity frequency change $\delta\omega$. It is however crucial to correctly simulate the distribution of mechanical amplitudes within the thermal mechanical state.

We have demonstrated the effects of the optomechanical nonlinearity in a system that operates in the regime $\sqrt{2\bar{n}_{\text{th}}}g_0/\kappa \gtrsim 1$, and described how it modifies the optical response, transduction, and backaction over a wide range of temperatures. It is to be expected that a growing number of optomechanical systems will operate in this regime as parameters continue to improve, and the single-photon strong coupling regime ($g_0 > \kappa, \Gamma$) is approached. Indeed, various characteristics of the nonlinear regime we demonstrate are reminiscent of the expected effects due to quantum fluctuations in the single-photon strong coupling regime, including a modification of the optical response and the appearance of strong higher-order sidebands in optical fluctuation spectra. Whereas our sliced photonic crystal nanobeam devices demonstrate these effects for the bad-cavity limit, the regime has equally important impact for devices in the resolved-sideband regime ($\kappa \ll \Omega_m$), although precise manifestations are expected to vary. In particular, the optical excitation spectrum will be altered by displaying multiple discrete sidebands, as analysed in the strong-coupling regime for ground-state motion in ref. [21]. Moreover, backaction forces acquire an additional delay factor due to the longer lifetime of cavity excitation, which will lead to fluctuating damping and driving forces affecting the motion. Notably, a combination of such dynamical backaction and the optomechanical nonlinearity could be used as a resource to manipulate thermal fluctuations beyond a Gaussian distribution. Similar aims in the bad-cavity limit could be reached through nonlinear measurement, such as the displacement-squared measurements we demonstrated.

Interestingly, the alteration of the optical response due to thermal motion provides a new method to directly determine the intrinsic optical linewidth κ and the optomechanical coupling rate g_0 : the ratio of different harmonics of the transduced mechanical spectrum allows retrieving the relative frequency fluctuations $\delta\omega_{\text{rms}}/\kappa$. Together with a measurement of the optical excitation linewidth (see Methods eq. 6) this uniquely determines both g_0 and κ . This

method only requires further knowledge of the bath temperature and the mechanical frequency. We note that there is no need for any other calibration, including characterization of optical powers.

The large single-photon cooperativity C_0 in the structures we present here offers prospects beyond the exploitation of the optomechanical nonlinearity, in particular for quantum measurement and control of mechanical motion. For example, the requirement for feedback cooling to the ground state (thermal occupancy below 1) is that the cooperativity $C_0 n_c > \bar{n}_{\text{th}}/(9\eta - 1)$, where n_c is the number of photons in the cavity^{5,50,51}. In our sliced nanobeam structure, the measurement sensitivity is currently limited by the collection efficiency, which we estimate to be $\eta \approx 1.3\%$ (see Appendix). The double-period modulation method we use to improve the coupling efficiency of a photonic crystal nanobeam cavity at normal incidence has previously been shown⁴¹ to yield a simulated collection efficiency of more than 20%. Therefore we expect that by either improving the optical design, or by employing waveguide-based coupling schemes^{49,51}, the coupling can be further increased in our current free-space set-up. For example, with a detection efficiency of 2/9, ground state preparation would be in reach at a very modest minimum cavity occupation of $n_c > 17$ photons with the demonstrated parameters. Finally, the large optomechanical coupling strength in combination with low loss provides other opportunities for measurement-based control in the bad-cavity limit, such as conditional state preparation of the mechanical resonator by pulsed measurements[52], or quantum state swapping between the optical and mechanical degrees of freedom[27].

Methods

Sliced photonic crystal nanobeam design

Eigenfrequency calculations were performed using finite element software (COM-SOL Multiphysics). For optical simulations, perfectly matched layers were used to allow the extraction of the optical radiation losses. To estimate $\partial\omega_c/\partial x$, the optical frequency shift due to mechanical motion, x (half of the gap size) was increased by 1 nm over the full length of the nanobeam, leading to a change in the simulated eigenfrequency.

The sliced nanobeam design confines light in the transverse direction due to total internal reflection, while along the nanobeam the photonic crystal patterning creates a bandgap for light. An optical cavity is formed by a defect region in the middle with holes of different shape and periodicity, which is tapered to the periodic outer region over 5 holes to minimize optical losses⁴⁰. Additionally, we create a low-efficiency outcoupling grating in the structure by making the hole sizes alternately 5% wider and narrower. This double-period modulation allows part of the cavity field to scatter out at normal incidence⁴¹, which is efficiently collected by our free-space optical measurement setup. Our experimental results indicate that this strategy increases the coupling efficiency to the optical cavity from approximately 0.1% to 1–2% (see Appendix).

Fabrication

Devices were fabricated from a silicon-on-insulator substrate (SOITEC), with a 250 nm silicon device layer on top of 3 μm silicon oxide. Patterns were written using e-beam lithography in a 80 nm layer of spincoated HSQ resist (FOX-15, Dow Corning) and developed using TMAH. The silicon layer was etched in an ICP plasma etcher using a combination of Cl_2 and HBr/O_2 gases. Finally, the nanobeams were released to be free-standing by wet etching with HF , which also dissolves leftover resist and oxide-based deposits formed during plasma etching. The wet etch was followed by critical point drying to prevent collapse of the nanobeams. The device layer of SOI wafers typically contains compressive stress, which can induce buckling of the nanobeams even when using critical point drying. We avoided this by incorporating stress-relief features in the support structure around the free-standing nanobeams.

Balanced homodyne detection at cryogenic temperatures

A closed-cycle cryostat (Montana Cryostation C2) was used to control the sample temperature between 3 and 300 K. We used an aspheric lens positioned outside the cryostat window with an effective focal length of 8 mm and a numerical aperture of 0.55 to focus the laser beam (New Focus Velocity 6725, linewidth ≤ 200 kHz) on the sample and to collect the reflection in free space. A balanced detector with two nominally identical photodiodes (New Focus 1817-FS) detected the output of the homodyne interferometer, schematically shown in Fig. 1c. The detector signal was then Fourier transformed and the spectrum recorded with an electronic real-time spectrum analyser (Agilent MXA). The optical power in the reference arm was 135 μW or more, ensuring that the optical shot noise was at least as large as the electronic noise. The pressure in the cryostat was typically 0.3 mbar at room temperature, and well below 10^{-4} mbar at cryogenic temperatures.

A measurement of the power dependence of the transduced signal (see Appendix) was performed to verify that the measurement of the thermal motion of the nanobeam is not influenced by additional heating by the laser beam. We then used the temperature sensor placed next to the sample in the cryostat to calibrate the scale for the displacement power spectral density S_{xx} in Fig. 2a and Fig. 4b.

Power spectral density and Voigt linewidth

We plot the power spectral density of the electronic output signal of our measurement setup, which has units of W/Hz . This corresponds to a power spectral density of a (virtual) optical power P , S_{PP} , which has units of W^2/Hz . As a consequence, the Lorentzian detuning dependence of the optomechanical transduction leads to a Lorentzian-squared dependence in the power spectral density. Similarly, we observe the square of the Gaussian distribution of cavity frequencies due to thermal motion. Therefore, we fit the square of a Voigt lineshape, which models the convolution of a Lorentzian and a Gaussian lineshape, to our data, and extract the linewidth of the non-squared Voigt lineshape. This value then directly corresponds to either the optical loss rate κ or the amplitude of the frequency fluctuations $\delta\omega_{\text{rms}}$, in the respective limits where $\kappa \ll \delta\omega_{\text{rms}}$ or

vice versa.

We use an empirical equation for the linewidth of a Voigt lineshape⁵³:

$$0.5346\kappa + \sqrt{0.2166\kappa^2 + 8 \ln 2 \delta\omega_{\text{rms}}^2}, \quad (6)$$

where κ is the linewidth of the Lorentzian lineshape and $2\sqrt{2 \ln 2} \delta\omega_{\text{rms}}$ is the linewidth of the Gaussian lineshape. To fit the linewidth as a function of temperature, we substitute $\delta\omega_{\text{rms}} = \sqrt{2g_0^2 kT / \hbar \Omega_m}$. To account for multiple independent mechanical modes, we can calculate the individual optomechanical coupling rates from the asymptote of the fit curve if we know the ratio between the transduced peaks in the spectrum³⁶. The variances due to the modes j add up, $\delta\omega_{\text{rms}}^2 = \sum_j \langle \delta\omega_j^2 \rangle$, which means Eq. 1 is modified to

$$\delta\omega_{\text{rms}}^2 = \sum_j \left(\frac{g_{0,j}^2}{\hbar \Omega_{m,j}} \right) 2k_B T. \quad (7)$$

Numerical model for higher-order transduction

Timetraces for the mechanical displacement x were generated for one or two resonance frequencies Ω_m . To simulate thermal motion, we randomly change the amplitude A and phase φ of harmonic motion $x = A \cos(\Omega_m t + \varphi)$. The points at which A and φ are changed are taken from a Poissonian distribution with mean time between jumps taken to be the mechanical damping time Γ . The new amplitude is taken from an exponential distribution characterized by a mean proportional to the average thermal occupation \bar{n}_{th} , while the phase is taken from a uniform distribution. A timetrace of the measurement output P was generated from the position timetrace using our full model for the transduction in the phase-averaged homodyne measurement, as given in the Appendix. The discrete Fourier transform of this timetrace allowed us to extract the signal strength at Ω_m and at higher-order multiples or mixing terms.

References

1. Aspelmeyer, M., Kippenberg, T. J. & Marquardt, F. Cavity optomechanics. *Rev. Mod. Phys.* **86**, 1391–452 (2014).
2. Chan, J. *et al.* Laser cooling of a nanomechanical oscillator into its quantum ground state. *Nature* **478**, 89–92 (2011).
3. Teufel, J. D. *et al.* Sideband cooling of micromechanical motion to the quantum ground state. *Nature* **475**, 359–63 (2011).
4. Verhagen, E, Deléglise, S, Weis, S, Schliesser, A & Kippenberg, T. J. Quantum-coherent coupling of a mechanical oscillator to an optical cavity mode. *Nature* **482**, 63–7 (2012).
5. Wilson, D. J. *et al.* Measurement-based control of a mechanical oscillator at its thermal decoherence rate. *Nature* **524**, 325–329 (2015).
6. Brooks, D. W. C. *et al.* Non-classical light generated by quantum-noise-driven cavity optomechanics. *Nature* **488**, 476–480 (2012).
7. Safavi-Naeini, A. H. *et al.* Squeezed light from a silicon micromechanical resonator. *Nature* **500**, 185–9 (2013).

8. Purdy, T. P., Yu, P.-L., Peterson, R. W., Kampel, N. S. & Regal, C. A. Strong Optomechanical Squeezing of Light. *Phys. Rev. X* **3**, 031012 (2013).
9. Wollman, E. E. *et al.* Quantum squeezing of motion in a mechanical resonator. *Science* **349**, 952–955 (2015).
10. Pirkkalainen, J.-M., Damskägg, E., Brandt, M., Massel, F. & Sillanpää, M. A. Squeezing of Quantum Noise of Motion in a Micromechanical Resonator. *Phys. Rev. Lett.* **115**, 243601 (2015).
11. Lecocq, F, Clark, J. B., Simmonds, R. W., Aumentado, J & Teufel, J. D. Quantum Nondemolition Measurement of a Nonclassical State of a Massive Object. *Phys. Rev. X* **5**, 041037 (2015).
12. Palomaki, T. A., Teufel, J. D., Simmonds, R. W. & Lehnert, K. W. Entangling Mechanical Motion with Microwave Fields. *Science* **342**, 710–713 (2013).
13. Palomaki, T. A., Harlow, J. W., Teufel, J. D., Simmonds, R. W. & Lehnert, K. W. Coherent state transfer between itinerant microwave fields and a mechanical oscillator. *Nature* **495**, 210–4 (2013).
14. Purdy, T. P., Peterson, R. W. & Regal, C. A. Observation of Radiation Pressure Shot Noise on a Macroscopic Object. *Science* **339**, 801–804 (2013).
15. Murch, K. W., Moore, K. L., Gupta, S. & Stamper-Kurn, D. M. Observation of quantum-measurement backaction with an ultracold atomic gas. *Nat. Phys.* **4**, 561–564 (2008).
16. Riedinger, R. *et al.* Non-classical correlations between single photons and phonons from a mechanical oscillator. *Nature* **530**, 313–316 (2016).
17. Sudhir, V. *et al.* Quantum correlations of light due to a room temperature mechanical oscillator for force metrology, arXiv:1608.00699 (2016).
18. Purdy, T. P., Grutter, K. E., Srinivasan, K. & Taylor, J. M. Observation of Optomechanical Quantum Correlations at Room Temperature, arXiv:1605.05664 (2016).
19. Kampel, N. S. *et al.* Harnessing quantum correlations for physics beyond the standard quantum limit in broadband displacement detection, arXiv:1607.06831 (2016).
20. Nunnenkamp, A., Børkje, K. & Girvin, S. M. Single-Photon Optomechanics. *Phys. Rev. Lett.* **107**, 063602 (2011).
21. Rabl, P. Photon blockade effect in optomechanical systems. *Phys. Rev. Lett.* **107**, 1–5 (2011).
22. Lemonde, M.-A., Didier, N. & Clerk, A. A. Enhanced nonlinear interactions in quantum optomechanics via mechanical amplification. *Nat. Commun.* **7**, 11338 (2016).
23. Doolin, C. *et al.* Nonlinear optomechanics in the stationary regime. *Phys. Rev. A* **89**, 053838 (2014).
24. Brawley, G. A. *et al.* Nonlinear optomechanical measurement of mechanical motion. *Nat. Commun.* **7**, 10988 (2016).

25. Vanner, M. R., Hofer, J, Cole, G. D. & Aspelmeyer, M. Cooling-by-measurement and mechanical state tomography via pulsed optomechanics. *Nat. Commun.* **4**, 2295 (2013).
26. Khosla, K. E., Vanner, M. R., Bowen, W. P. & Milburn, G. J. Quantum state preparation of a mechanical resonator using an optomechanical geometric phase. *New J. Phys.* **15**, 043025 (2013).
27. Bennett, J. S. *et al.* A quantum optomechanical interface beyond the resolved sideband limit. *New J. Phys.* **18**, 053030 (2016).
28. Kippenberg, T. J., Rokhsari, H., Carmon, T., Scherer, A. & Vahala, K. J. Analysis of Radiation-Pressure Induced Mechanical Oscillation of an Optical Microcavity. *Phys. Rev. Lett.* **95**, 033901 (2005).
29. Marquardt, F., Harris, J. G. E. & Girvin, S. M. Dynamical multistability induced by radiation pressure in high-finesse micromechanical optical cavities. *Phys. Rev. Lett.* **96**, 1–4 (2006).
30. Vahala, K *et al.* A phonon laser. *Nat. Phys.* **5**, 682–686 (2009).
31. Bagheri, M., Poot, M., Li, M., Pernice, W. P. H. & Tang, H. X. Dynamic manipulation of nanomechanical resonators in the high-amplitude regime and non-volatile mechanical memory operation. *Nat. Nanotechnol.* **6**, 726–732 (2011).
32. Krause, A. G. *et al.* Nonlinear Radiation Pressure Dynamics in an Optomechanical Crystal. *Phys. Rev. Lett.* **115**, 1–5 (2015).
33. Carmon, T., Cross, M. & Vahala, K. Chaotic Quivering of Micron-Scaled On-Chip Resonators Excited by Centrifugal Optical Pressure. *Phys. Rev. Lett.* **98**, 167203 (2007).
34. Wu, J. *et al.* Dynamical chaos in chip-scale optomechanical oscillators, arXiv:1608.05071 (2016).
35. Navarro-Urrios, D. *et al.* Nonlinear dynamics and chaos in an optomechanical beam, arXiv:1609.04390 (2016).
36. Leijssen, R. & Verhagen, E. Strong optomechanical interactions in a sliced photonic crystal nanobeam. *Sci. Rep.* **5**, 15974 (2015).
37. Meenehan, S. M. *et al.* Pulsed Excitation Dynamics of an Optomechanical Crystal Resonator near Its Quantum Ground State of Motion. *Phys. Rev. X* **5**, 041002 (2015).
38. Schilling, R. *et al.* Near-Field Integration of a SiN Nanobeam and a SiO₂ Microcavity for Heisenberg-Limited Displacement Sensing. *Phys. Rev. Appl.* **5**, 054019 (2016).
39. Brennecke, F., Ritter, S., Donner, T. & Esslinger, T. Cavity Optomechanics with a Bose-Einstein Condensate. *Science* **322**, 235–238 (2008).
40. Quan, Q. & Lončar, M. Deterministic design of wavelength scale, ultra-high Q photonic crystal nanobeam cavities. *Opt. Express* **19**, 18529 (2011).
41. Tran, N.-V.-Q., Combrié, S., Colman, P., De Rossi, A. & Mei, T. Vertical high emission in photonic crystal nanocavities by band-folding design. *Phys. Rev. B* **82**, 075120 (2010).
42. La Gala, G., Leijssen, R., Muhonen, J. & Verhagen, E. Quadrature-averaged homodyne detection of cavity frequency modulation. *in prep.*

43. Thompson, J. D. *et al.* Strong dispersive coupling of a high-finesse cavity to a micromechanical membrane. *Nature* **452**, 72–75 (2008).
44. Miao, H., Danilishin, S., Corbitt, T. & Chen, Y. Standard Quantum Limit for Probing Mechanical Energy Quantization. *Phys. Rev. Lett.* **103**, 100402 (2009).
45. Clerk, A. A., Marquardt, F. & Harris, J. G. E. Quantum Measurement of Phonon Shot Noise. *Phys. Rev. Lett.* **104**, 213603 (2010).
46. Paraïso, T. K. *et al.* Position-Squared Coupling in a Tunable Photonic Crystal Optomechanical Cavity. *Phys. Rev. X* **5**, 041024 (2015).
47. Kaviani, H. *et al.* Nonlinear optomechanical paddle nanocavities. *Optica* **2**, 271 (2015).
48. Vanner, M. R. Selective Linear or Quadratic Optomechanical Coupling via Measurement. *Phys. Rev. X* **1**, 021011 (2011).
49. Gröblacher, S., Hill, J. T., Safavi-Naeini, A. H., Chan, J. & Painter, O. Highly efficient coupling from an optical fiber to a nanoscale silicon optomechanical cavity. *Appl. Phys. Lett.* **103**, 181104 (2013).
50. Genes, C., Vitali, D., Tombesi, P., Gigan, S. & Aspelmeyer, M. Ground-state cooling of a micromechanical oscillator: Comparing cold damping and cavity-assisted cooling schemes. *Phys. Rev. A* **77**, 033804 (2008).
51. Krause, A. G., Blasius, T. D. & Painter, O. Optical read out and feedback cooling of a nanostring optomechanical cavity, arXiv:1506.01249 (2015).
52. Vanner, M. R. *et al.* Pulsed quantum optomechanics. *Proc. Natl. Acad. Sci. U.S.A.* **108**, 16182–7 (2011).
53. Olivero, J. & Longbothum, R. Empirical fits to the Voigt line width: A brief review. *J. Quant. Spectrosc. Radiat. Transf.* **17**, 233–236 (1977).

Acknowledgements

We thank Thijs Kleijntjens for assistance in setting up the balanced homodyne interferometer. This work is part of the research programme of the Netherlands Organisation for Scientific Research (NWO). E.V. gratefully acknowledges an NWO-Vidi grant for financial support. J.T.M. thankfully acknowledges funding from the European Union’s Horizon 2020 research and innovation programme under the Marie Skłodowska-Curie grant agreement No 707364.

Appendix

Balanced homodyne interferometric measurement of an optomechanical cavity

The optical response of the balanced homodyne interferometer probing our cavity optomechanical system is a function of the average detuning $\bar{\Delta}$ between the laser frequency and the cavity frequency, the frequency shift of the cavity due to mechanical motion $\delta\omega$, the homodyne phase θ , the cavity linewidth κ , and various constant factors such as the coupling efficiency to the cavity, and the optical power used for the measurement. To obtain the full expression, we start by describing the reflection from our nanobeam cavity using input-output theory:

$$s_c = s_{\text{in}} \left(ce^{i\phi} - \frac{\eta\kappa}{i\Delta + \kappa/2} \right), \quad (\text{S1})$$

with η the coupling efficiency. The term $ce^{i\phi}$ is due to non-resonant scattering from the nanobeam structure or the substrate. If ϕ is 0, the resulting reflectivity shows a Lorentzian response, while other values will lead to the more general case of a Fano lineshape.

Using balanced homodyne detection, with the light in the reference arm, or local oscillator, described as $s_{\text{LO}} = |s_{\text{LO}}|e^{i\theta}$ and the input to the cavity s_{in} taken to be real, the output of the detector is proportional to a virtual optical power P :

$$\begin{aligned} \frac{P}{\hbar\omega} &= \left| \frac{i}{\sqrt{2}}s_c + \frac{1}{\sqrt{2}}s_{\text{LO}} \right|^2 - \left| \frac{i}{\sqrt{2}}s_{\text{LO}} + \frac{1}{\sqrt{2}}s_c \right|^2 \\ &= i(s_{\text{LO}}s_c^* - s_{\text{LO}}^*s_c) \\ &= |s_{\text{LO}}||s_{\text{in}}| \left(-2c\sin(\theta - \phi) + \frac{\eta\kappa(2\Delta\cos\theta + \kappa\sin\theta)}{\Delta^2 + \kappa^2/4} \right). \end{aligned} \quad (\text{S2})$$

Finally, we can substitute $\Delta \equiv \bar{\Delta} + \delta\omega = \bar{\Delta} + \frac{\partial\omega}{\partial x}x$ to obtain the relationship between the measurement output P and the displacement x .

Optomechanical transduction with order-by-order approximation

We consider the Taylor expansion of the measurement output P for small fluctuations $\delta\omega$ around $\bar{\Delta}$:

$$P(\bar{\Delta} + \delta\omega) = P(\bar{\Delta}) + \sum_{k=1}^{\infty} \frac{\delta\omega^k}{k!} \frac{\partial^k P}{\partial\omega^k}. \quad (\text{S3})$$

For harmonic fluctuations $\delta\omega = \delta\omega_0 \cos \Omega_m t$, the individual terms of this expansion contribute at different frequencies. To leading order, $\cos^k \varphi = \frac{1}{2^{k-1}} \cos k\varphi$, which means the higher-orders are completely spectrally separated, and we can consider this expansion *order by order*.

We measure the power spectral density $S_{PP}(\Omega)$, whose integral over frequency gives the variance $\langle P^2 \rangle$. Averaging over the homodyne phase, the detuning dependence for $(\partial^k P / \partial\omega^k)^2$ has a simple Lorentzian lineshape, raised

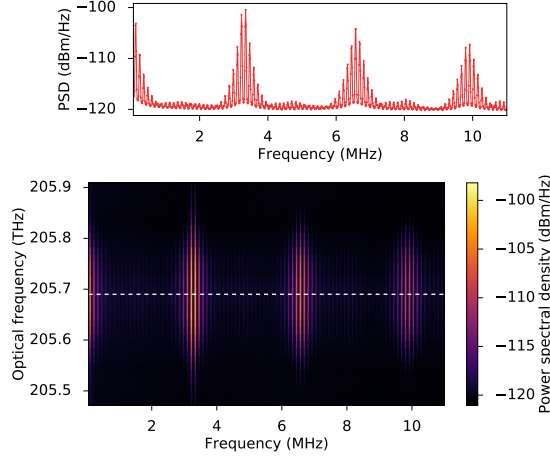


Figure S1 | Nonlinear transduction. Electronic spectrum analyser signal taken at room temperature, as a function of the optical frequency.

to the power $(k + 1)$, as we analyze elsewhere¹. The maximum contribution is therefore at resonance ($\bar{\Delta} = 0$) and can be expressed as

$$\left(\frac{\partial^k P}{\partial \omega^k}\right)^2 = A^2 k!^2 \left(\frac{2}{\kappa}\right)^{2k}, \quad (\text{S4})$$

where $A^2 = 8P_{\text{in}}P_{\text{LO}}\eta^2$ is a constant prefactor that depends on the optical powers $P_{\text{in}}, P_{\text{LO}}$ in the signal and reference arm, respectively, and on the coupling efficiency to the cavity η .

We now calculate the band power at a frequency $k\Omega_m$, where only the k th term of the Taylor expansion contributes, as

$$\langle P^2 \rangle_{k\Omega_m} \equiv \int_{k\Omega_m} S_{PP} d\Omega = A^2 \left(\frac{2}{\kappa}\right)^{2k} \langle (\delta\omega^k)^2 \rangle_{k\Omega_m} \quad (\text{S5})$$

Since $\delta\omega = (\partial\omega_c/\partial x) \delta x$, we can use the properties of the higher moments of x . For thermal motion, and again using the order-by-order approximation^{2,3}, we use

$$\langle (x^k)^2 \rangle_{k\Omega_m} = \frac{k!}{2^{k-1}} \langle x^2 \rangle^k, \quad (\text{S6})$$

which we can directly substitute into Eq. S5 to obtain

$$\langle P^2 \rangle_{k\Omega_m} = 2A^2 k! \left(\frac{2\langle \delta\omega^2 \rangle}{\kappa^2}\right)^k, \quad (\text{S7})$$

which we used in the main text.

The nonlinear transduction as a function of detuning can be seen in the spectrogram in Fig. S1. The crosscut corresponds to Fig. 3a in the main text. Due to the quadrature-averaging homodyne detection, all peaks show a single-peaked detuning dependence which is maximum at resonance.

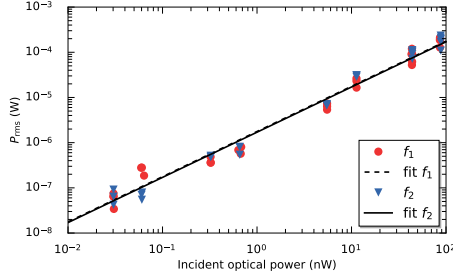


Figure S2 | Power dependence. Measured band power of the two fundamental mechanical frequencies f_1 and f_2 as a function of the incident optical power, with the laser frequency on-resonance with the cavity.

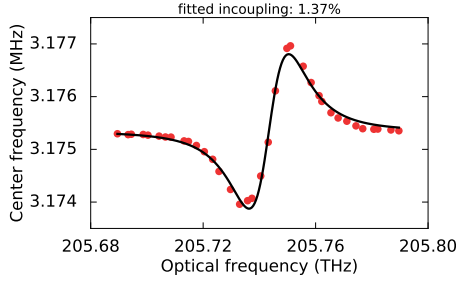


Figure S3 | Optical spring effect at low temperature. Center frequencies of one of the peaks in the mechanical spectra with the structure at 3 K.

Power dependence of transduced mechanical motion

The transduction of mechanical motion depends on the optical power used, as shown in the dependence of $\langle P^2 \rangle$ on $A^2 \propto P_{\text{in}} P_{\text{LO}}$ in Eq. S7. In particular, we expect the measured band power to be linear in both the power in the signal arm P_{in} , incident on the cavity, and the power in the reference arm P_{LO} . Deviations from a linear relation indicate heating or cooling of the mechanical motion due to the additional laser power⁴. Figure S2 shows transduced mechanical motion as a function of the incident optical power, with the laser on-resonance with the cavity and while the device was cooled to 3 K. The data was corrected for the local oscillator power, which was mostly kept constant and did not vary by more than a factor 10. At higher powers (near 100 nW), fluctuations in the center frequency and shape of the peak could be observed (similar to the effects shown off-resonance in Fig. 5 in the main text), however the peak area still follows the linear dependence as a function of the optical power incident at the structure. This shows that for all probe powers used here, there is no significant heating due to the incident laser light.

Estimation of coupling efficiency from the optical spring effect

Figure S3 shows the fitted center frequency of the mechanical resonance f_1 at 3 K with $P_{\text{in}} = 20.6$ nW, corresponding to the spectrogram shown in Fig. 5a

in the main text. Fitting the change in frequency as a function of the optical detuning with the function describing optical spring effect in the bad-cavity limit^{4,5} provides us with an estimate of the incoupling efficiency. The average over 5 measurements at different input power yielded a coupling efficiency $\eta = 1.3\%$, with a standard deviation of 0.3%.

This analysis ignores the effects of the large thermal fluctuations, which as we show in the main text broadens and reduces the strength of the optical spring effect. This means the obtained coupling efficiency provides a lower limit for the actual coupling efficiency. However, the numerical model we used to generate the simulated spectra in Fig. 5 in the main text shows that the fluctuations at 3 K mainly broaden the mechanical spectra but don't yet lead to strong reduction in the strength of the optical spring effect.

Radiation pressure force in a cavity with large thermal fluctuations

We express the radiation pressure force in the cavity as

$$F_{\text{rad}} = \frac{\hbar(\partial\omega_c/\partial x)n_c^{\text{max}}}{1 + u^2}, \quad (\text{S8})$$

where $u \equiv \frac{2}{\kappa}(\bar{\Delta} + (\partial\omega_c/\partial x)x)$ and n_c^{max} is the maximum number of photons in the cavity when it is driven at resonance. We assume the resonator moves harmonically: $x(t) = x_0 \sin \Omega t$. This results in a time-dependent normalized detuning $u(t) = \bar{u}(\bar{\Delta}) + u_0 \sin \Omega t$, where $u_0 = 2(\partial\omega_c/\partial x)x_0/\kappa$.

Given an amplitude x_0 , we extract the first fourier coefficient of the force (at the resulting harmonic frequency Ω):

$$a_1^{\text{rad}} = \frac{\Omega}{\pi} \int_0^{2\pi/\Omega} F_{\text{rad}}(t') \sin \Omega t' dt'. \quad (\text{S9})$$

In analogy with the mechanical restoring force, we can calculate an effective spring constant from the fourier coefficient: with $F = -kx$ and $x(t) = x_0 \sin \Omega t$, $F = \sum_{n=1}^{\infty} a_n \sin n\Omega t$ implies that $a_1 = -kx_0$.

Finally, a correction on the spring constant results in a correction on the frequency Ω :

$$\Omega = \sqrt{\frac{k + k_{\text{rad}}}{m}} = \sqrt{\frac{k}{m}} \sqrt{1 + \frac{k_{\text{rad}}}{k}}, \quad (\text{S10})$$

which we can approximate using $\sqrt{1+x} \approx 1 + x/2 + \dots$:

$$\Omega \approx \sqrt{\frac{k}{m}} \left(1 + \frac{k_{\text{rad}}}{2k}\right), \quad (\text{S11})$$

therefore

$$\delta\Omega \approx \sqrt{\frac{k}{m}} \frac{k_{\text{rad}}}{2k} = \frac{k_{\text{rad}}}{2m\Omega}. \quad (\text{S12})$$

To obtain the results presented in Fig. 5 in the main text, we perform this calculation for a large number of amplitudes x_0 , sampled from a thermal distribution. We then average together Lorentzian lineshapes with center frequencies given by the resulting set of frequency shifts.

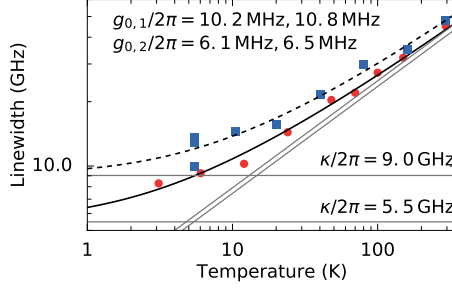


Figure S4 | Characterisation of a second device. Linewidth versus temperature data, similar to Fig. 2d in the main text. For the dataset with blue squares, the sample was not shielded from thermal radiation.

Characterization of a second device

The data labeled as “device 2” was taken on a sample with a slightly different design, which did not include the double-period modulation to increase the outcoupling, as well as a different shape of the holes. The optical linewidth as a function of temperature for this device is shown in Fig. S4, in two separate datasets. The dataset shown with blue squares was taken with only one window in the cryostat, which was at room temperature, such that the sample was not shielded from thermal radiation. The other dataset was taken with the second window (cooled to around 10 K) in place. Therefore the sample temperature for the blue dataset was most likely higher than the thermometer temperature, which we used to plot and fit this data. Although this leads to a relatively large difference in the fitted optical loss rate κ , both datasets yield very similar coupling rates g_0 .

Quadratic displacement measurements

The signal-to-noise ratio (SNR) of a quadratic displacement measurement, in the regime where the order-by-order approximation is valid, can be found by considering Eq. S7, and assuming the measurement is shot-noise limited. If the optical power in the reference arm is much larger than in the signal arm of the interferometer ($P_{LO} \gg P_{in}$), the power spectral density due to the optical shot noise is given by $S_{PP}^{SN} = \hbar\omega_c P_{LO}$. The band power at $2\Omega_m$ due to thermal mechanical fluctuations is given by Eq. S7, with $k = 2$ and $\langle \delta\omega^2 \rangle = 2\bar{n}_{th}g_0^2$, leading to

$$\langle P^2 \rangle_{2\Omega_m} = 512P_{in}P_{LO}\eta^2 \left(\frac{g_0}{\kappa} \right)^4 \bar{n}_{th}^2, \quad (S13)$$

where we also substituted $A^2 = 8P_{in}P_{LO}\eta^2$. The power spectral density will show a Lorentzian peak with linewidth 2Γ at the frequency $2\Omega_m$, which means its peak value is related to the band power (area under the peak) as $S_{PP}^{max} = \langle P^2 \rangle_{k\Omega_m} / 2\Gamma$. Finally, we take the signal-to-noise ratio

$$\text{SNR} \equiv \frac{S_{PP}^{max}}{S_{PP}^{SN}} = 256 \frac{P_{in}/\hbar\omega_c}{\Gamma} \eta^2 \left(\frac{g_0}{\kappa} \right)^4 \bar{n}_{th}^2 \quad (S14)$$

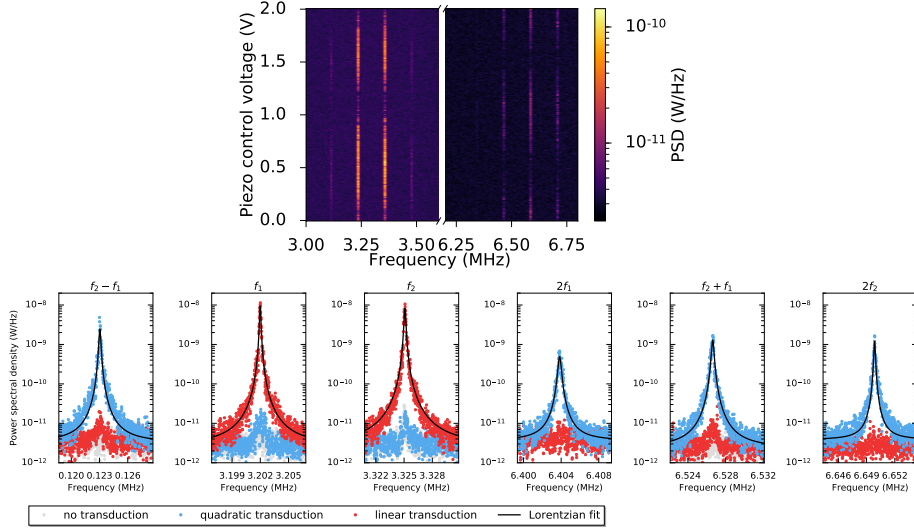


Figure S5 | Selective linear and quadratic measurement. Top: spectra showing the first and second order transduction obtained simultaneously, as a function of the piezo mirror position. Bottom: maximum and minimum linear and quadratic transduction at different settings of the homodyne phase, for all first- and second-order peaks. Incident optical power was 12.8 nW.

and set it to 1 to find the minimum detectable average phonon occupation $n_{\min} \equiv \min(\bar{n}_{\text{th}})$, leading to

$$\frac{1}{\bar{n}_{\min}} = 16 \left(\frac{g_0}{\kappa} \right)^2 \eta \sqrt{\frac{P_{\text{in}}/\hbar\omega_c}{\Gamma}}. \quad (\text{S15})$$

Figure S5 shows additional data for the quadratic measurement presented in the main text. The top panel shows the peak around the fundamental frequency decrease at the same piezo mirror position where the peaks at twice the frequency are strongest, further confirming the ability to suppress the linear measurement while performing the quadratic measurement. The bottom panel shows the linear and quadratic measurements at optimum positions of the piezo mirror for both fundamental frequencies and all 4 second-order combinations.

References

1. La Gala, G., Leijssen, R., Muhonen, J. & Verhagen, E. Quadrature-averaged homodyne detection of cavity frequency modulation. *in prep.*
2. Brawley, G. A. *et al.* Nonlinear optomechanical measurement of mechanical motion. *Nat. Commun.* **7**, 10988 (2016).
3. Hauer, B., Maciejko, J. & Davis, J. Nonlinear power spectral densities for the harmonic oscillator. *Ann. Phys. (N. Y.)* **361**, 148–183 (2015).
4. Aspelmeyer, M., Kippenberg, T. J. & Marquardt, F. Cavity optomechanics. *Rev. Mod. Phys.* **86**, 1391–452 (2014).

5. Leijssen, R. & Verhagen, E. Strong optomechanical interactions in a sliced photonic crystal nanobeam. *Sci. Rep.* **5**, 15974 (2015).